Modelling urban meteorology with increasing refinements for the complex morphology of a typical Chinese city (Xi'an)

Xi Zhang [a,b,*], Gert-Jan Steeneveld [b], Dian Zhou [a], Reinder J. Ronda [b], Chengjiang Duan [a], Sytse Koopmans [b], Albert A.M. Holtslag [b]

[a] *School of Human Settlements and Civil Engineering, Xi'an Jiaotong University, No.99 Yanxiang Road, Xi'an, Shaanxi Province, China*
[b] *Meteorology and Air Quality Section, Wageningen University, P.O. Box 47, 6700 AA Wageningen, the Netherlands*

ARTICLE INFO

ABSTRACT

Urban areas are vulnerable to intensive heatwave periods. In order to understand heat stress in cities, the single-layer urban canopy model (SLUCM) coupled with the weather research and forecasting model (WRF) have been widely used to quantify and forecast the urban climate. However, the model performance in WRF/SLUCM is limited by the coarse classification of urban canopy parameters (UCPs), and further improvements may require great effort. Therefore, this study was a new attempt at organizing the gridded UCPs in the 'National Urban Database and Access Portal Tool (NUDAPT) approach' and exploring its application in the WRF/SLUCM model in four simulations with contrasting UCP configurations. The model performances were evaluated for a heatwave period in 2018 in the typical Chinese city of Xi'an, using a near-surface observational network consisting of 39 meteorological stations in various urban spatial categories. We found that the increased accuracy in UCPs brought about gradual and overall improvements in the urban heat island effect (UHI) and air temperature (Ta), and had relatively slight effects on absolute humidity ($\rho\nu$) and wind speed (WP). Furthermore, the station-to-station bias analyses indicated that optimization efficiency varied among urban spatial categories. Areas with an open form or areas densely covered with vegetation showed constant sensitivity to the increasing refinements of UCPs. Input of the gridded and multi-dimensional descriptions of urban canyon geometry contributed to more accurate results in dense urban areas and areas with mixed and inhomogeneous morphology.

1. Introduction

Heatwave periods, which are increasing in frequency, intensity and duration due to climate change, pose a threat to human health and safety [1]. In urban areas, elevated temperatures caused by high-density constructions and impervious pavements negatively affect outdoor thermal comfort and promote heat-related illnesses [2–5]. To alleviate urban heat stress and help develop mitigation strategies, studies on urban climate, urban heat island effects, and thermal comfort have received more attention in recent years [6–8]. An accurate qualification and urban climate prediction could provide much needed support for these studies [9,10].

Currently, the weather research and forecasting model (WRF) is one of the most advanced numerical weather prediction systems [11] and it is also a suitable modeling method for mesoscale weather simulations [12]. Considering the effects of the urban canopy layer, the single-layer urban canopy model (SLUCM) coupled with the WRF model could estimate the transfer of energy and momentum between an urban surface and the atmosphere and provide reliable simulations of urban areas [13].

However, accurate quantification of the urban climate using WRF/SLUCM is currently still a challenge [9]. In the early attempts at WRF/SLUCM modeling, all urban areas were uniformly set with the same urban canopy parameters (UCPs). This was too simplistic to represent the urban geometry and it was later replaced by three urban land-use types. Previous studies illustrated that using a three land-use class strategy could improve the model performance [14–16], with more realistic turbulent energy partitioning and urban boundary layer (UBL) height [17]. Unfortunately, in heterogeneous cities experiencing rapid development, the three land-use class strategy may lead to distortions of urban spatial characteristics and overestimations of nocturnal air temperature and surface wind speed [15–17]. Therefore, a

---

more detailed input of UCPs in WRF/SLUCM is needed to correct for the inaccurate description of urban morphological classification and to improve the model performance in WRF/SLUCM.

Recently, the digital parameterization of urban morphology has become more straightforward with the development of remote-sensing techniques and spatial statistics methods. Some neighborhood scale studies have extracted the building typologies and urban textures from typical residential areas or downtown districts and applied it in the UWG [18,19] or CFD [20] program to simulate the urban climate condition. Parametric simulations and sensitivity analysis are used to reveal the relative impacts of urban characteristics, building systems and building design strategies on the estimates of urban air temperature, urban energy consumption [18,19] and vertical velocity [20].

Meanwhile, for larger city scale studies, UCP datasets with high resolutions covering the built-up areas, like the National Urban Database and Access Portal Tool (NUDAPT) [21], are available for an increasing number of cities and these could be applied to WRF/SLUCM simulations. To date, few studies have discussed the SLUCM model results based on NUDAPT data due to the lack of direct input of UCPs. Alternatively, NUDAPT data are applied in the multi-layer urban canopy scheme, e.g. the Building Effect Parameterization (BEP) and Building Energy Model (BEM) [22–24]. Otherwise, the NUDAPT data are partly used in the SLUCM model, i.e., by only taking the urban fraction into account to improve the model results of air temperature [16,25,26]. The improvements that could be realized by using more detailed UCPs on WRF/SLUCM performance have not yet been fully revealed.

In this study, we provided a transformation from the urban 3D building dataset into the gridded UCP dataset in the NUDAPT approach for Xi'an (China), suitable for the WRF/SLUCM model. We carried out four sensitivity simulations with contrasting levels of UCP configurations, from one or three class datasets to gridded UCP data. The model performance was evaluated against observed air temperature at 2 m (Ta), 10-m wind speed, absolute humidity at 2 m ($\rho\nu$) and the urban heat island intensity at 2 m (UHI). In addition, a high-density observational network containing 39 stations with various urban spatial categories was used for further station-to-station model evaluation in order to reveal the optimization efficiency in various urban spatial categories. Note that the universality and representativeness of these spatial categories in a typical Chinese city as Xi'an were proved in our previous study [27].

The description of the WRF/SLUCM and designing sensitivity simulations are presented in Section 2. Comparison of model results and surface variables are discussed in Section 3, and the associated Student t-tests to prove the statistical significance of these differences are presented in the Appendix (Tables S2 and S3). The discussion in Section 4 explores the limitation and representativeness of the results and proposes the possibly further studies. Conclusions are discussed in section 5.

2. Materials and methods

2.1. Modelling system

This study used the integrated WRF/urban modeling system (version 3.7.1) coupled with the single-layer urban canopy model (SLUCM), which was embedded within the Noah-LSM scheme of WRF [11]. In the modeling efforts on coupling SLUCM, the urban fraction (FRC_URB), which specifies the fraction of the surface that is covered by impervious material in a grid cell, played an important role [13]. More specifically, the calculations of surface fluxes and surface temperature were executed separately for two tiles (Fig. 1), i.e. the impervious surface was provided by the SLUCM model and the so-called natural surface by the Noah LSM model. These two independent results were then weighted and summed to obtain the combined result. The FRC_URB was used as the weighting factor. Considering the obvious differences in the composition of surface energy fluxes between impervious and natural surfaces, the FRC_URB could have directly influenced the grid result.

Furthermore, within the impervious part of a grid cell, the urban morphology was simplified and made into an infinitely long street canyon (Fig. 1), which consisted of three urban surfaces (roof, wall, and roads), for which the surface energy budgets were separately solved [13]. Also, the internal physical processes like shadowing, reflections, and trapping of radiation were considered in the SLUCM model. The rationale behind the use of more detailed UCPs originates in building a more accurate and representative urban canyon in the SLUCM model, which may effectively improve the modeling performance.

2.2. Input approach of urban canopy parameters in WRF/SLUCM

Two approaches were used to specify the UCPs in the WRF/SLUCM to present the canyon geometry. The first one was the traditional lookup table, which classified the urban areas into three land-use types mainly according to the urban fraction (FRC_URB): (1) low-density residential (LI) with a value of 0.3–0.8, (2) high-density residential (HI) with a value of 0.8–1, (3) commercial or industrial (COI) indicating all highly developed areas not classified as HI. The table also related the average value of *basic morphological indicators* of three land-use types, like building height (ZR), building width (BW), street width (SW), anthropogenic heat flux (AH) and so on. In this approach, it would be hard to avoid the underestimation of urban morphological heterogeneity, especially in a city with complex and diverse spaces.

To compensate for this, the gridded-UCPs approach provided each grid cell in the city with a unique combination of UCPs. The gridded-UCPs dataset presented *advanced morphological indicators* in the NUDAPT way, which were not available in the table approach, such as plan area fraction, area-weighted mean building height, building surface
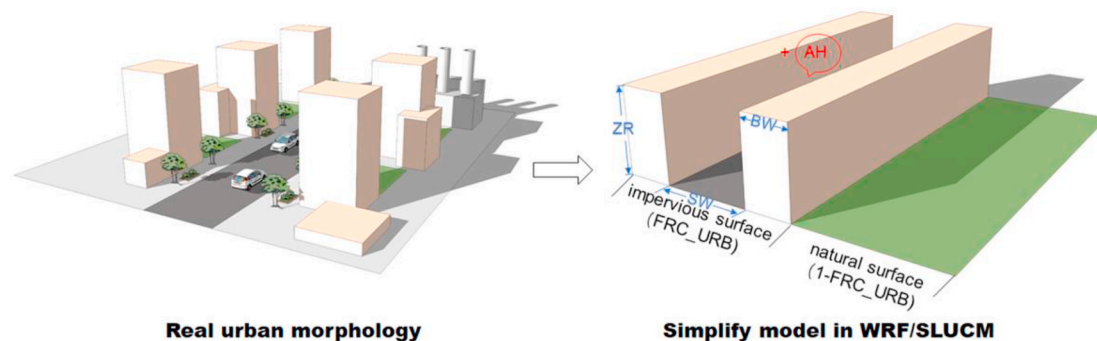

Real urban morphology   **Simplify model in WRF/SLUCM**

Fig. 1. Schematic of the WRF/SLUCM model, presenting the coupling process of the SLUCM and LSM models. In each grid cell, the area proportion of the impervious surface was FRC_URB, and the natural surface was 1-FRC_URB. The real urban morphology was simplified to an infinitely long street canyon, which is defined with ZR (mean building height), BW (mean building width) and SW (mean road width) in meters. The value of AH (anthropogenic heat) as traffic and industry emissions were taken from the lookup table, according to land-use types.

to plan area ratio and frontal area indexes for 8 directions [21]. These indicators were not only used to redefine the calculation of three urban surfaces, but also provided multi-dimensional information for the parameterized canyon geometry.

2.3. Model configuration

The study area is Xi'an (33.4–34.5°N, 107.4°-109.5°E), a typical Chinese city and the capital of the Shanxi province (Fig. 2). Xi'an experienced a warm and dry summer (June, July and August) with a mean temperature of 27.1 °C between 2014 and 2017 [28]. The central urban area of Xi'an covered an urban constructional area of 460 km^2 and supported a population of 4.67 million in 2016 [28]. The local topography with hills in the north and east surrounding the city restricts the diffusion of heat. The UHI effect was prominent in Xi'an with a maximum intensity of 9 K in July [29].

The heatwave period, from the 18th to the 26th of July 2018, was selected to carry out the model experiment. According to the meteorological record spanning the past five years, this heatwave period presented ideal circumstances for our study with a relatively long duration and a prominent diurnal temperature cycle. (Fig. 3a). Since the UHI is one of the key indicators discussed in this study, we selected weather conditions favorable for the UHI. A few days with a short-time rainfall at the beginning and at the end of the heatwave period have been excluded, so that the clear sky and calm wind situations would dominate the simulation period. This approach excluded effects of model deficiencies due to cloud cover and high wind speeds and improved the accuracy of sensitive experimental results, only for the conditions that were critical.

Based on the comprehensive consideration of computational cost and model performance, we adopted the re-initialization strategy in this study, which refered to a series of short-time simulation integrations. This was needed since one long weather forecast would likely be vulnerable to errors since the synoptic scale weather conditions may have differed in the model as compared to the observations on that time scale. More specifically, the WRF model was re-initialized every 72 h, so the whole simulation process consisted of four individual runs (Fig. 3b). The first 24 h in the simulation were spin-up and removed. A total of 168 h (from LST 2018/7/19 0:00 to LST 2018/7/26 00:00) of simulation results were used in the analysis. The re-initialization strategy more accurately simulated the nocturnal temperature and contributed to an overall high correspondence with observations (Fig. 3c), which was consistent with the findings of Jänicke et al. [26]. Other important model settings are displayed in Table 1.

Three nested domains were set up and the third one contained the Xi'an city which we focused on (Fig. 2). The original data for land use and land cover were obtained from the United States Geological Survey (USGS), with a spatial resolution of 1°. Considering Xi'an is a city experiencing rapid development, the USGS data originating from 1991

may have presented a delayed description of the current land-use characteristics. Hence, some detailed adjustments were carried out according to the latest remote sensing land-use data from Tsinghua University (FROM-GLC 2017) [30]. For example, the urban fraction (FRC_URB) in the third domain was derived from the FROM_GLC 2017 data with a resolution of 30 m and re-summarized to 1 km by using ArcGIS.

2.4. Experimental set-up

UCPs used in this study were derived from the urban digital 3D building dataset, which was provided by the Department for Architecture of Xi'an Jiaotong University [27]. First, all UCPs were summarized as gridded data with the resolution of 1 km^2. Then, the basic lookup approach was used to note the average value of three land-use types, but only for *basic morphological indicators* (Table 2). In the gridded-UCP dataset, additional calculations of *advanced morphological indicators* were carried out and all gridded canyon geometries were reparametrized and provided to the model. The derivations of these indicators in two approaches are presented in the Appendix (Table S1). The AH values applied in the simulations were the average values of three land-use types [31], with the exception of 1U which took the average value of Xi'an city.

A total of four sensitivity simulations were used to evaluate the sensitivity of UCP accuracy on the SLUCM model performance (Fig. 4). They were defined with the gradual accuracy of UCP configuration and other settings were consistent. The UCPs used in the first two simulations were found in the lookup table. While 1U homogenized the whole urban area as high-density residential (HI), 3U adopted three land-use types. The third simulation (3U + FRC) employed a mixture input approach, taking the gridded urban fraction while the other UCPs remained the same as in 3U. The last simulation (NU) utilized all data from the gridded UCPs dataset for the central urban area of Xi'an. 3U + FRC had more horizontally detail information than 3U, to specify the impervious proportion in each grid (Fig. 4). NU had also gained more 3D building information than 3U + FRC, which helped for more accurate descriptions of urban canyon geometry.

2.5. Derivation of urban wind speed from direct model output

Considering the urban canopy effects on the urban surface wind, the extraction of model results of 10-m wind was divided into two parts. The wind speeds at rural stations were directly exported by the WRF model and those at urban stations were calculated using the urban canopy wind profile following MacDonald (2000) [32]. The hourly grid-scale wind direction was determined using the WRF results at the first eta model level (approximately 104 m above the surface), which was also used as the reference to the corresponding frontal area index (λ_f). Based on λ_f, the empirical constants for the straight canyon pattern (as used in
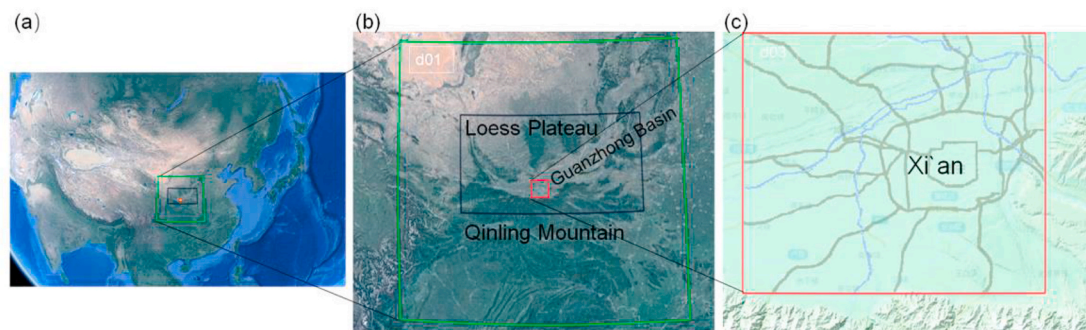

Fig. 2. (a) Map of China with the location of Domains. (b) Locations of Guanzhong Basin, and locations of Domain 1 and Domain 2. (c) The location and topography of Xi'an, which is also the Domain 3. The blue lines indicate the rivers and grey lines the roads. Source: GoogleMaps $^{(R)}$. (For interpretation of the references to color in this figure legend, the reader is referred to the Web version of this article.)
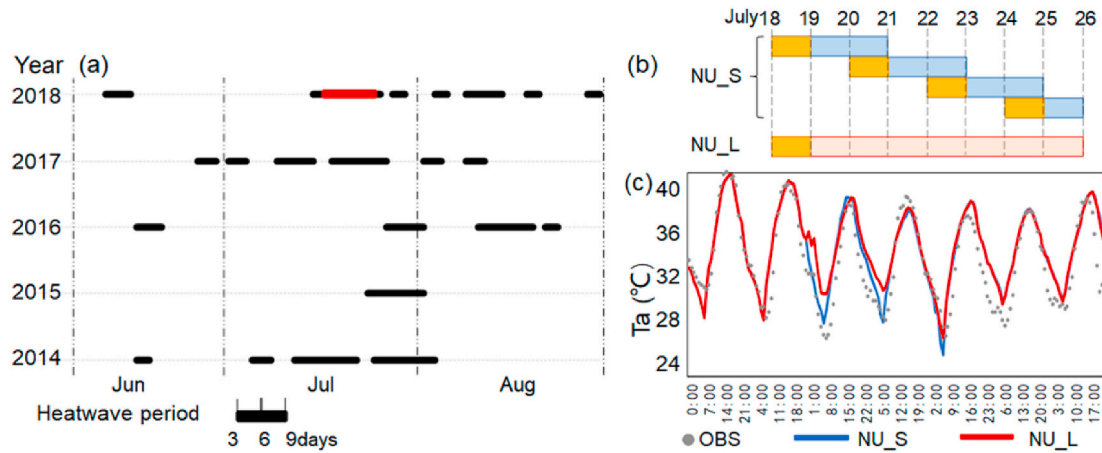
Fig. 3. (a) The summary of duration and frequency of heatwave periods in Xi'an, from 2014 to 2018. The black bar indicates the heatwave period and the red bar indicates the simulation period used in this study. (b) Schematic of the re-initialization strategy (NU_S). The blue bars indicate the four short-time simulations in NU_S, and red bars indicate the 7-day simulation in NU_L. The first 24-h of each simulation were spin-up and marked in yellow. (c) The comparison of hourly modeled Ta from July 19–25, 2018 in XGX station. The blue line indicates the result of the re-initialization strategy (NU_S), and the red line is the result of the 7-day simulation (NU_L). See Fig.5 for site locations. (For interpretation of the references to color in this figure legend, the reader is referred to the Web version of this article.)

Table 1
Summary of model settings.

General Setting	
Time (UTC)	Total duration: 2018.7.18 00:00–2018.7.26 00:00
	Four re-initialization simulations S1: 2018.7.18 00:00–2018.7.21 00:00 S2: 2018.7.20 00:00–2018.7.23 00:00 S3: 2018.7.22 00:00–2018.7.25 00:00 S4: 2018.7.24 00:00–2018.7.26 00:00
Grid setting	D1:68*68, resolution:15kmD2:201*111, resolution:3kmD3:61*61, resolution:1 km
Vertical resolution	35 eta level
Initial & boundary conditions	1°*1° six-hourly ECMWF data
Parameterizations	
Land Surface	NOAH
Boundary layer	MRF
Microphysics	WSM3 simple ice
Longwave radiation	Rrtm
Shortwave radiation	Dudhia

Table 2
Summary of Xi'an UCP data in the land-use table (URBPARM.TBL).

LU_INDEX	COI	HI	LI
FRC_URB (%)	0.94	0.86	0.67
ZR(m)	17.5	15.8	14.1
SIGMA_ZED(m)	17.2	15.7	13.1
ROOF_WIDTH(m)	11.2	11.8	13.5
ROAD_WIDTH(m)	10.2	12.2	23.1
AH (W/m²)	50	40	15

WRF/SLUCM) were determined from Table 4 [32]. These constants and the modeled wind speed at the first eta-level were used in Equation (1) to calculate the friction velocity (u^*) and the wind speed at the height which the individual obstacles were not influencing the wind (u_{z_w}), and Equation (2) to calculate the wind speed at obstacle roof height (u_H) [32]:

$$u_z = \frac{u^*}{k} \ln\left(\frac{z - d}{z_0}\right) \tag{1}$$

Here, u_Z (m/s) is the wind speed at the height of first eta level or the height at which the individual obstacles are not influencing the wind. k is a constant known as the von Kàrmàn constant ($k \approx 0.4$), d (m) is the zero-plane displacement, and z_0 (m) is the roughness length.

$$u_H = u_{z_w} - \frac{u^*}{B} \ln\left(\frac{A + Bz_w}{A + BH}\right) \tag{2}$$

Here, A and B are experimentally determined using Table 4, z_w (m) is the height which the individual obstacles are not influencing the wind, H (m) is the roof height of obstacles.

Finally, the results of wind speed at these key heights were used to diagnose the 10-m wind speed inside the urban canopy according to equation (3) [32]:

$$u_{10} = u_H e^{\left(9.6\lambda_f\left(\frac{10}{H}-1\right)\right)} \tag{3}$$

Here, u_H (m/s) is the wind speed at obstacle roof height H (m), and λ_f is the frontal area index.

What we need to stress here is that the λ_f played vital roles in the calculations above and directly influenced the results of 10-m wind speed. The calculation of λ_f is differently set in the land-use table and gridded dataset. In the table, λ_f assumes a uniform value of normalized building height (h) instead. In the gridded dataset, λ_f was calculated in four wind direction regimes (0°/180°,45°/225°,90°/270°,135°/315°) according to its definition. We could infer that the λ_f from the lookup table was less accurate and affected the subsequent model results for wind speed. This was reflected in the diagnostic 10-m wind speeds using the λ_f from the table approach, which were always less than 0.2 m/s and obviously different from the observations. We explored the possible interference of inaccurate λ_f input in the WRF/SLUCM model. Since the modeled results of wind speeds at the height of the first eta level were nearly the same in all simulations, the WRF/SLUCM model may not have been influenced by the data source of λ_f. Therefore, to obtain more reliable results of diagnostic 10-m wind speeds, we took the actual values of λ_f from the gridded dataset and consistently applied them in the four simulations.

2.6. Observations for model validation

The simulation results were evaluated using a high-density local meteorology observation network, provided by the Xi'an Meteorological Bureau (Fig. 5). This network contains 39 stations, 38 of which record the air temperature (Ta, °C). 26 stations record wind speed (WP, m/s) and 20 stations provide relative humidity data which was later converted to absolute humidity (ρν, g/m³). A few stations had missing observation data, details of which can be seen in Table S4. The
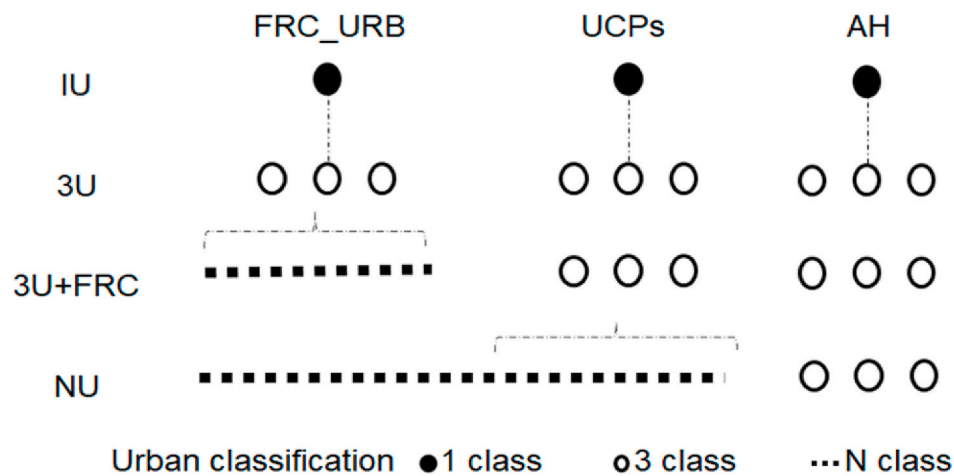
Fig. 4. Schematic of UCP configuration in four sensitivity simulations. The solid dot indicates one urban class, three hollow dots indicate three urban classes, and the dashed line indicates the data was not classified and each grid cell had a specific value.
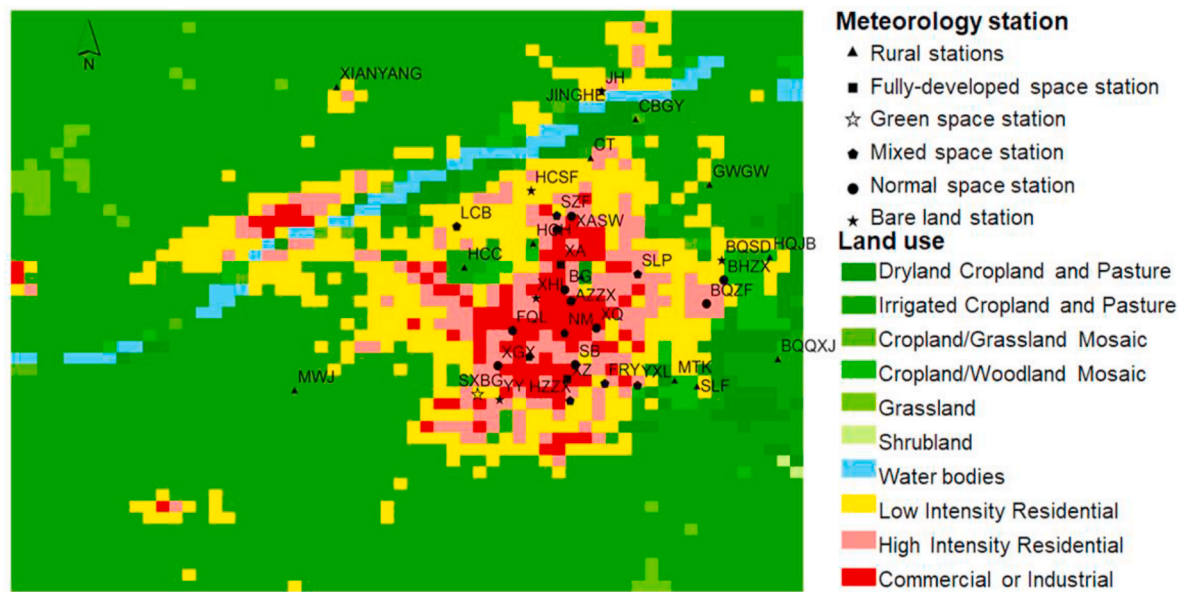

Fig. 5. The land-use of Xi'an according to FROM-GLC 2017. The locations of meteorological stations are identified and the shapes indicate various spatial categories.

instruments employed in this observational network were CAWS600RE, DZZ4 and CAWS600RT, with measuring error ranges of $-0.3\,°C \leq \triangle T \leq 0.3\,°C$ and $-0.2\,m/s \leq \triangle V \leq 0.2\,m/s$ [33]. The sensors measuring air temperature and relative humidity were located 2 m above the ground and recorded instantaneous per minute values. The 60-min records were averaged to obtain hourly observed Ta and relative humidity, which was consistent with the modeled results. The sensors of wind were situated 10 m from the ground and recorded instantaneous per second values.

The hourly average wind speed was the 2-min moving average closest to the full hour over an interval of 1 s. The detailed information concerning the metadata and surrounding photos of these stations were presented in a previous paper [27].

This network contains 12 rural stations, 6 of which were located in historical ruins or undeveloped areas inside the city. The other 26 urban stations were classified into three land-use types, 9 stations for LI and COI respectively, and 8 for HI (Table 3). We found that these urban

Table 3
Summary of land-use type and spatial category of urban stations.

Land_use type	Name	Spatial categories	Land_use type	Name	Spatial categories	Land_use type	Name	Spatial categories
LI	BQSD	Bareland	HI	XHL	Bareland	COI	NM	Mixed
	HCSF	Bareland		YY	Bareland		XQ	Normal
	JH	Bareland		DZKD	Mixed		BG	Normal
	SXBG	Green		YXL	Mixed		SB	Normal
	HZZX	Mixed		SLP	Mixed		AZZX	Normal
	SZF	Mixed		FQL	Normal		XAZX	Normal
	FRY	Mixed		BQZF	Normal		XASW	Normal
	LCB	Mixed		XGX	Normal		XZ	Fully-developed
	BHZX	Normal					XA	Fully-developed

stations could be subdivided according to the urban morphological characteristics, which further supports the station-by-station evaluations of the UCPs sensitivity in the WRF/SLUCM model.

Consistent with the strategy used in the UCP configuration, we retained the indicators of urban fraction and canyon geometry as key variables to predict the spatial categories. We adopted our previous classification method of urban spatial categories [27], using the vegetation fraction (Fveg) which is the opposite of the FRC-URB and sky-view factor (SVF). Therefore, the 26 urban stations were classified as Mixed space (SVF + Fveg>1), Normal space (0.6 ≤ SVF + Fveg≤1) and fully-developed Space (SVF + Fveg<0.6) [27]. Green space (Fveg >0.4) and Bare land (SVF>0.9) were added here to complete the system. The distribution and detailed information about the spatial categories of these stations are presented in Fig. 5 and Table 3 respectively.

3. Results

3.1. Surface air temperature

In this study, we used the 2-m air temperature (Ta) as the reference air temperature. The overall root mean squared error (RMSE) of Ta in 1U was 1.76 °C and the median absolute error (MEAE) was 1.14 °C, and that in 3U was to 1.77 °C and 1.15 °C (Table 5). According to these results and comparing them with the results from other cities [14–16], we could infer that the WRF/SLUCM model performed reasonably well in Xi'an. We found that the further efforts of fine-resolution UCPs contributed to improvements in overall model Ta performance, especially for the urban stations. The RMSE of urban stations in the 3U + FRC was 1.68 °C and improved by 1.61 °C in NU (Table 5). Additionally, the statistical significance of these improvements were established using the Student t-tests found in Tables S2 and S3.

These improvements were dominated by a decreased modeled Ta at night, which was normally overestimated in the urban area [16,17]. The time series of Ta for four stations with various land-use types (Fig. 6) indicate that the model performed uniformly well during the daytime with biases within the range of ±0.2 °C. However, more obvious differences in the four simulations appeared at night. For example, at the SZF station for the LI land-use type (Fig. 6), the average bias at night was 1.85 °C in 1U, which was 1.96 °C at LST 6:00 a.m. The overestimation of nocturnal Ta was slightly corrected in 3U and 3U + FRC, with an average error of 1.68 °C and 1.52 °C, respectively. While the NU simulation showed a more sensitive reaction to cooling effects during the night, the average error further dropped by 0.11 °C. The modeled minimum temperature was not overestimated in NU, and the modeled error decreased to −0.41 °C.

The evaluation of the overall Ta simulation, based on hourly results from all stations, presented progressive changes from 1U to the NU. This means that we could carry out a hierarchical evaluation of all stations according to their bias analysis, as stations with large errors (RMSE>2 °C), stations with medium errors (1.6 °C < RMSE<2 °C), and stations with minor errors (RMSE<1.6 °C). Fig. 7 showed that the percentage of

Table 4
Calculated dimensionless values of several parameters for straight pattern of obstacles [32].

λ_f	d/H	z_w/H	z_0/H	A/H	B
0.05	0.066	2	0.048	−0.35	0.56
0.11	0.26	2.5	0.071	−0.35	0.5
0.16	0.32	2.7	0.084	−0.34	0.48
0.2	0.42	1.5	0.08	−0.56	0.66
0.33	0.57	1.2	0.077	−0.85	0.92

Here, λ_f is the frontal area index, d (m) is the zero-plane displacement, and H (m) is the roof height of obstacles. z_w (m) is the height which the individual obstacles are not influencing the wind, z_0 (m) is the roughness length. A and B are experimental constants.

Table 5
Summary of model performance of various UCP configurations in four surface meteorological indicators.

Variable	Type	Indicators	1U	3U	3U + FRC	NU
Ta(°C)	Overall	RMSE	1.76	*1.77*	1.69	**1.65**
		MEAE	1.14	*1.15*	**1.07**	**1.07**
	Rural stations	RMSE	*1.77*	1.76	**1.73**	**1.73**
		MEAE	1.18	*1.23*	1.21	**1.17**
	Urban stations	RMSE	1.75	*1.77*	1.68	**1.61**
		MEAE	*1.13*	1.11	**1.02**	1.03
WP(m/s)	Overall	RMSE	1.65	1.67	*1.68*	**1.62**
		MEAE	0.84	0.84	0.85	**0.83**
	Rural stations	RMSE	2.22	*2.26*	*2.26*	**2.17**
		MEAE	1.35	*1.41*	1.31	**1.30**
	Urban stations	RMSE	**1.30**	1.31	*1.32*	**1.29**
		MEAE	**0.69**	**0.69**	*0.70*	*0.70*
$\rho\nu$(g/m³)	Overall	RMSE	*3.36*	3.34	3.33	**3.28**
		MEAE	*2.47*	2.45	2.44	**2.39**
	Rural stations	RMSE	**3.05**	*3.07*	*3.07*	**3.05**
		MEAE	**2.02**	2.09	2.04	*2.10*
	Urban stations	RMSE	*3.47*	3.44	3.43	**3.38**
		MEAE	*2.66*	2.61	**2.57**	2.58
UHI (°C)	Overall	RMSE	*1.61*	1.56	1.54	**1.47**
		MEAE	*1.02*	0.99	0.99	**0.94**
	Daytime	RMSE	**1.57**	*1.61*	1.59	*1.61*
		MEAE	**1.03**	1.09	1.07	1.07
	Nighttime	RMSE	*1.67*	1.49	1.47	**1.25**
		MEAE	*1.00*	0.85	0.89	**0.79**

The RMSE is the abbreviation of the root mean squared error, and the MEAE is the median absolute error. The daytime period is LST 7:00~20:00, which is after sunrise and before sunset. The nighttime is LST 21:00~6:00. Best performance in four simulations is indicated in bold, and worst performance in italic.

stations with a large error had 16% in 1U, decreasing to 14% in 3U, 11% in 3U + FRC and 8% in NU. Also, the largest RMSE among these stations dropped from 2.74 °C in 1U–2.18 °C in NU (Fig. 7a). Taking a closer look at the individual effects of contrasting UCP configurations, we noticed that the modeled performances of Ta were similar in 1U and 3U. This indicated that the UCPs categorized according to land-use had no added value in our study due to the complexity and diversity of the urban morphology in Xi'an. The gridded urban fraction in 3U + FRC accurately specified the surface evapotranspiration of these areas and improved the model performance, the percentage of stations with minor errors increasing from 14% in 3U–32% in 3U + FRC. The second improvement of the modeled Ta benefited from the gridded building information in NU, which was weaker but more comprehensive. 32.5% of stations had a better result compared with that in 3U + FRC, and the proportion of stations with large errors further decreased to 11%.

In addition, a station-to-station bias analysis indicated that optimization effects may have differed between stations with various land-use types (Fig. 7b). Generally, stations with the land-use attribute LI benefited more than other stations, the RMSE falling by an average of 0.2 °C per simulation from 1U to NU (Fig. 7b). This effect may be explained by the morphology of these LI stations, since most of them are open space or parkland, which were classified as Green space, Bare land and Mixed Space in this study. Meanwhile, the HI and COI stations mainly consisted of Normal space and Fully-developed space, the gradient decrease of RMSE from 1U to 3U + FRC was less than 0.05 °C, and from 3U + FRC to NU was about 0.1 °C in some stations.

First, to explain the improvements for the LI stations, we noticed their actual FRC_URB values deviated greatly from the values used in 1U, which was the average for the whole city. Thus, the corrections of FRC_URB with the average of three land-use types in 3U, partly avoided the misrepresentation of surface energy balance fluxes, according to the calculation principle of the WRF/SLUCM model. Considering flux observations were lacking for Xi'an, and the modeled Ta in NU showed closer agreement with the observed Ta, the modeled fluxes in NU were used to evaluate the performance of the other three simulations. Taking a typical Bare-land station (e.g. BQSD), the hourly mean surface sensible
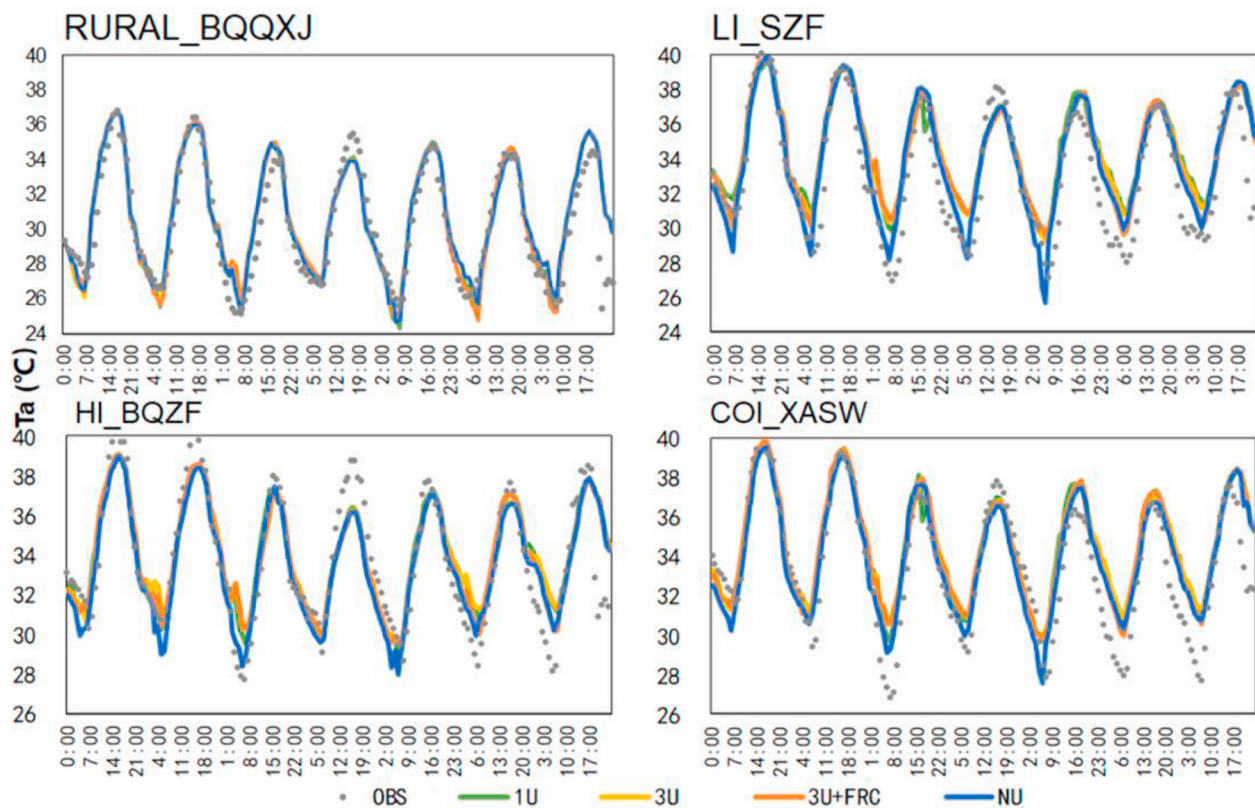
Fig. 6. Time series of hourly Ta in four representative stations with various land-use types, from July 19–25, 2018. The grey dots indicate the observation, and lines indicate the modeled results. See Fig.5 for site locations.
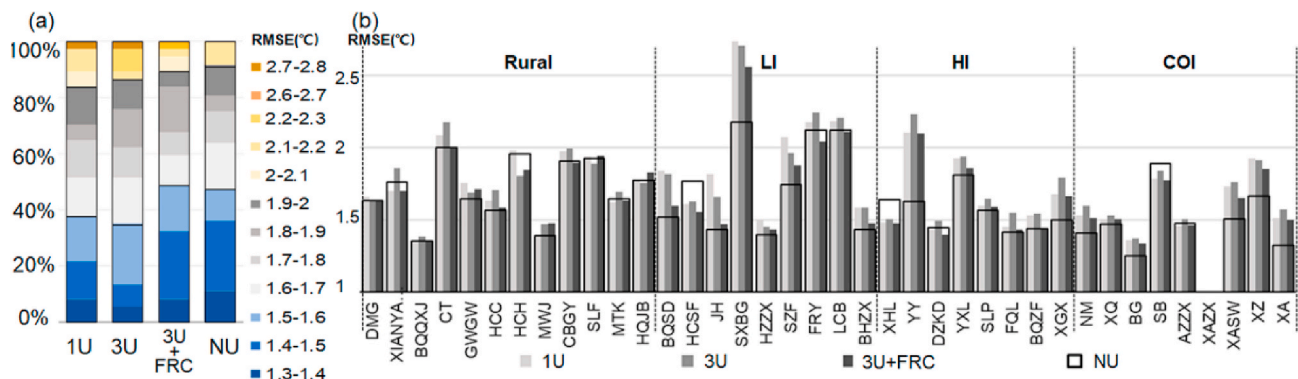

Fig. 7. The comparison of Ta modeled performance in four simulations: (a) Cumulative relative frequency indicates the result of the hierarchical evaluation of all stations, according to their bias analysis. Stations with large errors (RMSE>2 °C) are yellow, stations with medium errors (1.6 °C < RMSE<2 °C) are grey, and stations with minor errors (RMSE<1.6 °C) are blue. (b) All 38 stations were divided into one rural and three urban classes, the results of four simulations at each station are represented by bars of different colors. See Fig. 5 for site locations. (For interpretation of the references to color in this figure legend, the reader is referred to the Web version of this article.)

heat flux and latent heat flux are displayed in Fig. 8a. As BQSD was located in an open park, its actual FRC_URB was 0.61. This was much lower than the average value in 1U of 0.86, but close to that in 3U of 0.68, according to the LI land-use. Consequently, the calculated sensible heat flux in 1U was overestimated by 36–80 W/m^2 during the daytime, and 11–40 W/m^2 at night (Fig. 8a). Compared with results using gridded UCPs, the results of sensible heat flux in 3U were nearly credible. The further improvements appeared in 3U + FRC adopting the actual FRC_URB as 0.61, with a more accurate simulation of latent heat. Especially for daytime, the underestimated latent heat flux in 1U had a 20–110 W/m^2 rise in 3U, and 6–36 W/m^2 further rise in 3U + FRC. We found similar improvements in the Mixed Space stations, such as for the

SZF station (Fig. 8b) and we will skip a repetitive discussion here.

Secondly, the improvements of model performance for the HI and COI stations were determined by the gridded UCPs provided in NU, especially the *advanced morphological indicators*. Since most of the HI and COI stations were classified as Normal space, which are widely distributed in Xi'an city, the actual values of *basic morphological indicators* were close to those found in the land-use table. For example, for XGX station, we found similar surface heat fluxes in 1U, 3U and 3U + FRC (Fig. 8c), because of the same FRC_URB value in the land-use table and gridded dataset. However, this station had a special form with large-scale buildings and wider roads, which was quite different from the morphology summarized in the land-use table using *advanced*
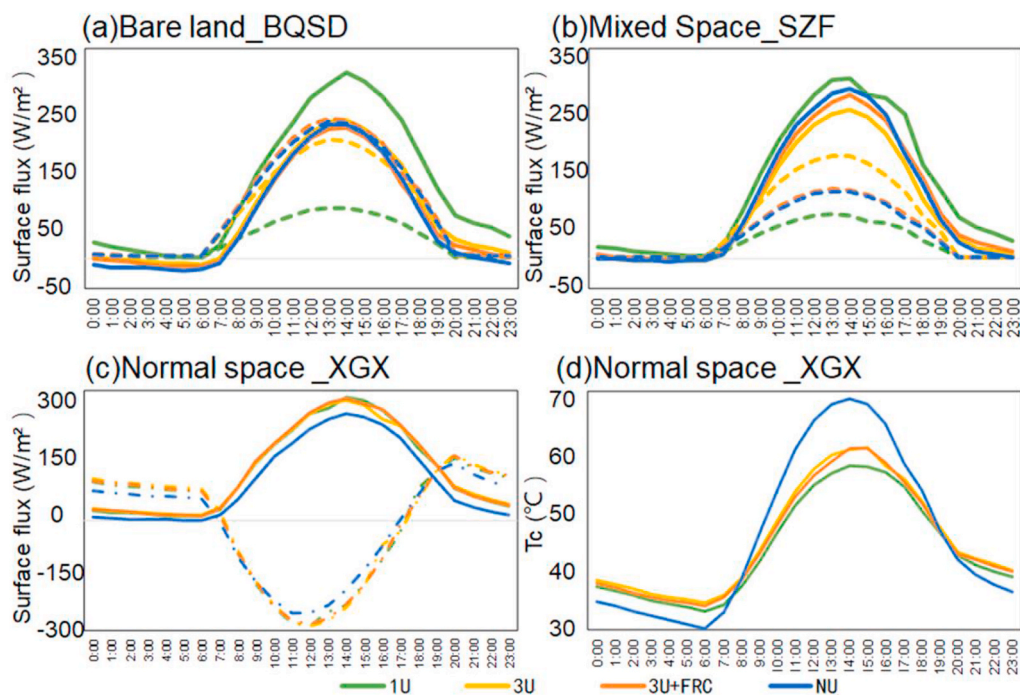
Fig. 8. (a) and (b) are the time series of 7-day average surface fluxes of two representative stations, classified into Bare-land space and Mixed space, respectively. The solid line represents sensible heat flux, and the dash line latent heat flux. (c) is the time series of 7-day average surface flux inside the canopy in the XGX station, which is Normal space. The solid line represents sensible heat flux and dash line storage heat flux. (d) is the time series of 7-day average canopy temperature in the XGX station. See Fig.5 for site locations.

morphological indicators. Once the added information in NU provided a more accurate canyon representation in the WRF/SLUCM model, the results of surface-related variables as sensible heat fluxes and ground heat fluxes became more reliable. More specifically, the sensible heat fluxes and storage heat fluxes declined by 20 W/m² in NU (Fig. 8c), due to the lower absorption of radiation by the relatively broad roads. Consequently, the canyon temperature (Tc) in NU showed different trends as compared with other simulations. Tc reached its daytime maximum at 14:00 LST, which was 10 K higher than others, and the nocturnal Tc was 5 K lower at night (Fig. 8d). Similar improvements due to gridded UCPs in NU also occurred in the Fully-developed space, and we will not repeat the description here.

3.2. Surface wind

Generally, the model performances for wind speed were similar in the four simulations and the NU showed slightly better results with an RMSE of 1.62 m/s and an MEAE of 0.83 m/s (Table 5). Fig. 9a showed

that the number of stations with a relatively small error (RMSE < 1.4 m/s) was more in NU and nearly the same in the other three simulations, and fewer stations with relatively high errors (RMSE >3.4 m/s) appeared in 3U + FRC and NU (Fig. 9a). The results in 3U and 3U + FRC implied the possibly negative effects brought by the three land-use class strategy in modeled wind speed, especially for urban stations.

According to the station-to-station bias analysis in Fig. 9b, we found the most improvements for rural stations, especially in the historical ruins (DMG station), remaining villages inside the city (HCC station), and the urban parks (YY station and FRY station). These stations had relatively open forms and were sparsely built. The horizontal mixings were negatively affected by the surrounding urban areas. According to the time series in Fig. 10, NU had a more stable performance due to the accurate morphological description of these stations and the surroundings. The modeled wind speed in NU remained mainly within the range of 0.5–4 m/s and was rarely more than 5 m/s, which was the most consistent with the observations. By comparison, stations with more buildings, like Normal space and Fully-developed space, did not have
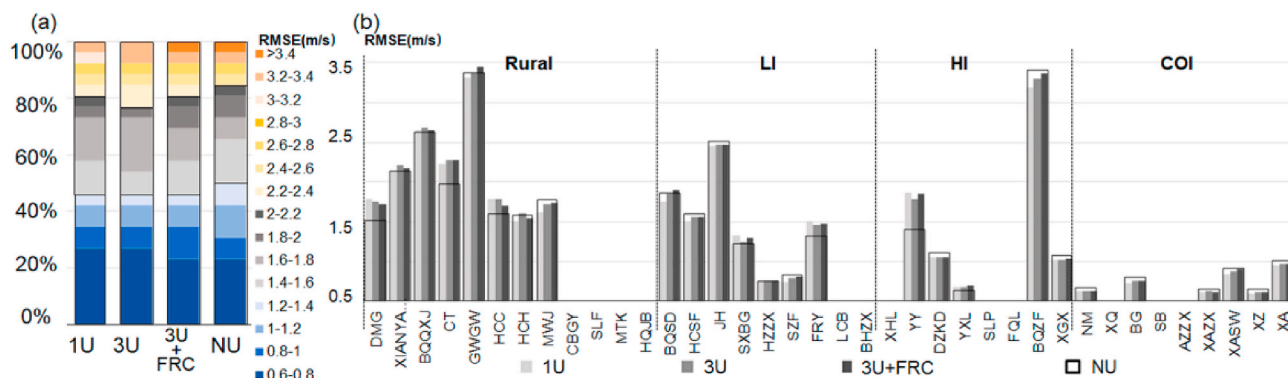

Fig. 9. The comparison of wind speed modeled in four simulations: (a) Cumulative relative frequency indicates the result of the hierarchical evaluation of all stations, according to their bias analysis. Stations with large errors (RMSE >2.2 m/s) are yellow, stations with medium errors (1.4<RMSE <2.2 m/s) are grey, and stations with minor errors (RMSE <1.4 m/s) are blue. (b) All 26 stations were divided into one rural and three urban classes, the results of four simulations at each station are represented by bars of different colors. See Fig. 5 for site locations. (For interpretation of the references to color in this figure legend, the reader is referred to the Web version of this article.)
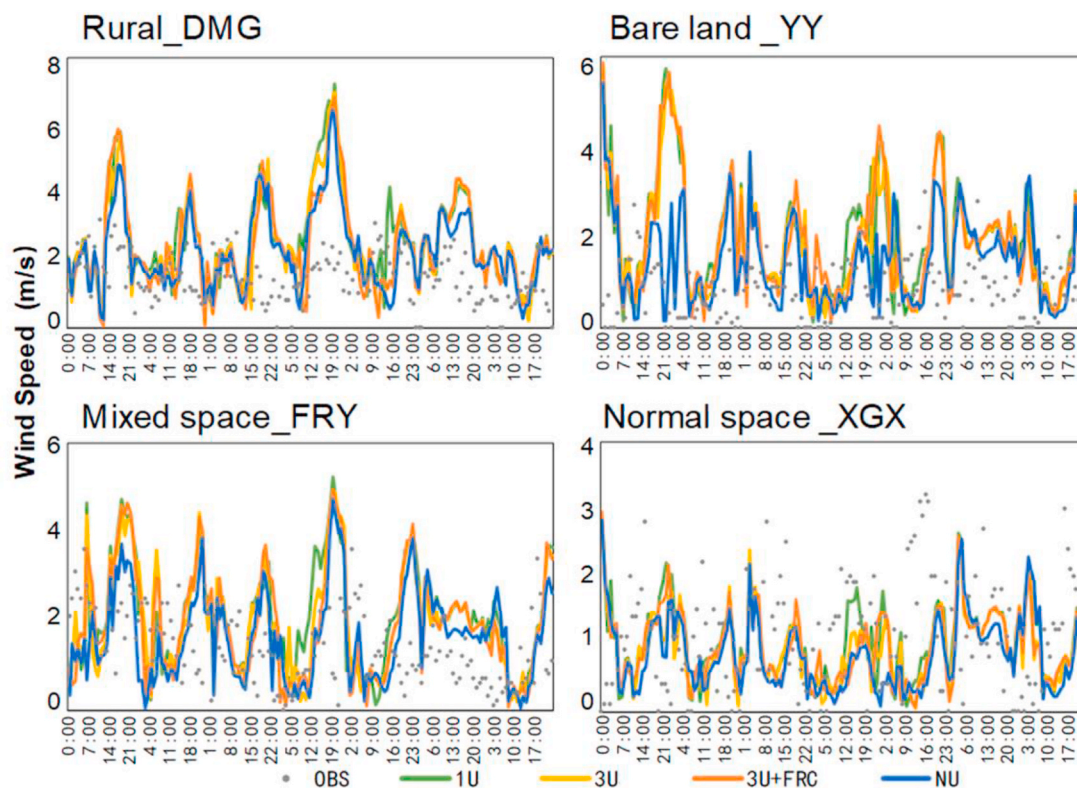
Fig. 10. Time series of hourly wind speed in four representative stations with various spatial categories, from July 19–25, 2018. The grey dots indicate the observation and lines indicate the modeled results. See Fig.5 for site locations.

better results in NU. For example, in XGX station, the deviations of modeled wind speed in the four simulations were typically less than 0.3 m/s, and sometimes the results in NU were underestimated by 1 m/s at night (Fig. 10).

3.3. Surface humidity

To eliminate the influence of air temperature and other climatic factors, we adopted the absolute humidity ($\rho\nu$,g/m³) at 2 m to compare the model performance of humidity in this study. The overall results of 1U, 3U and 3U + FRC were similar with an RMSE around 3.34 g/m³. NU was better with an RMSE of 3.28 g/m³ and an MEAE of 2.39 g/m³ (Table 5).

This improvement from 1U to NU was also seen in the station-to-station bias analysis presented in Fig. 11a. The total number of stations with minor errors (RMSE <2.5 g/m³) and medium errors (2.5<RMSE <4 g/m³) were the same in 1U, 3U and 3U + FRC. Only in NU did the number of stations with large errors (RMSE > 4 g/m³) experience a small decrease of 10% (Fig. 11a). Furthermore, we found that most stations had a smaller bias in NU. From 1U to NU, the minimum bias declined from 2.01 g/m³ to 1.98 g/m³, while the maximum RMSE declined from 4.7 g/m³ to 4.66 g/m³. Similarly, the sum of stations with an RMSE less than 2 g/m³ experienced a 10% increase, and those with an RMSE more than 4 g/m³ fell accordingly.

More specifically, the most prominent improvements of $\rho\nu$ in NU were found for the urban stations, especially for the Green space (SXBG
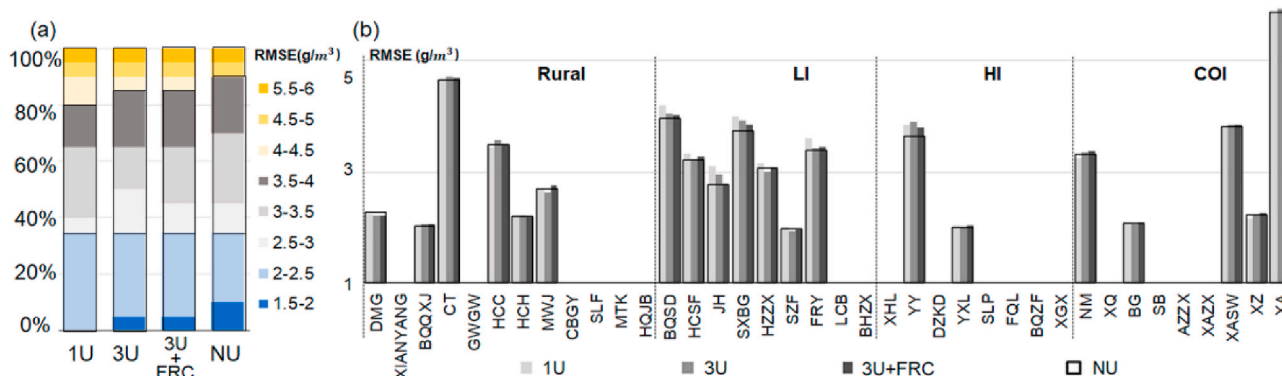

Fig. 11. The comparison of $\rho\nu$ modeled performance in four simulations: (a) Cumulative relative frequency indicates the result of the hierarchical evaluation of all stations, according to their bias analysis. Stations with large errors (RMSE>4 g/m³) are yellow, stations with medium errors (2.5<RMSE <4 g/m³) are grey, and stations with minor errors (RMSE <2.5 g/m³) are blue. (b) All 20 stations were divided into one rural and three urban classes, the results of four simulations at each station are represented by bars of different colors. See Fig. 5 for site locations. (For interpretation of the references to color in this figure legend, the reader is referred to the Web version of this article.)

station), Mixed space (FRY station) and Bare-land space (JH and YY station) (Fig. 11b). These spaces were urban parks or undeveloped suburban areas, with a vegetation fraction of more than 20%. Compared to other urban areas, these stations were highly covered by grass, shrubs and trees, which led to enhanced evapotranspiration. The gridded UCPs in the NU could have helped to modify the urban fraction and canyon geometry in these stations, which could have contributed to more accurate results of energy flux partitioning. The SXBG station experienced a gradual improvement, with RMSE decreasing from 4 g/m^3 in 1U–3.92 g/m^3 in 3U, and from 3.84 g/m^3 in 3U + FRC to 3.75 g/m^3 in NU (Fig. 11b). However, when Normal space and Fully-developed space where highly paved by impervious material, the results of the modeled ρv were consistent among the four simulations.

3.4. Urban heat island

3.4.1. The comparison of model performance of UHI intensity

In this study, the UHI effect refers to the 2-m air temperature difference between rural and urban environments. To calculate the UHI intensity, a suitable rural station was needed first. The selection of the rural station was based on three requirements: complete observation records, appropriate distance from the urban area, and located in the open countryside. The XIANYANG and the BQQXY station qualified (Fig. 12a). The next step of selection was to minimize the warming effects brought by urban heat advection (UHA) in the rural station. According to the time series of the air temperature and the wind direction (Fig. 12b and c), the UHA effect was detected in the XIANYANG station in all simulations. Five nights during the modeled period, the XIANYANG station located downwind of Xi'an city, had overestimated modeled Ta values. The BQQXJ station met the requirements and the UHA effect appeared only shortly during one night in 3U and 3U + FRC. Finally, the BQQXJ station was used as the rural reference station in this study, and showed a high correspondence of Ta with the observations.

The modeled UHI intensity showed a substantial sensitivity to contrasting UCP configurations, especially at night (after sunset and before

sunrise, LST 21:00–6:00). In 1U, because of the higher modeled Ta in urban areas, the nocturnal UHI intensities were overestimated with an RMSE of 1.67 °C (Table 5), which was consistent with previous studies [16,17]. With the input of *basic morphological indicators* in 3U, the overestimated UHI was effectively modified and the RMSE reduced by 0.18 °C, and the RMSE in 3U + FRC was 1.47 °C (Table 5). The *advanced morphological indicators* in NU improved the model performance of UHI, and the RMSE decreased to 1.25 °C (Fig. 13a).

Accordingly, the improvements in overall model performance were also reflected in each station. There was a general uptrend in the proportion of stations with minor error (RMSE<1.4 °C) of the total number, which increased from 48% in 1U–68% in 3U, up to 84% in NU (Fig. 13b). Although few stations had worse results in 3U + FRC, the model performance of most stations remained the same as 3U, and the maximum error decreased by 0.1 °C. The station-to-station bias analysis revealed that Mixed space, Green space and Bare-land Space had an average of 0.23 °C decrease from 1U to 3U (Fig. 13c). The gridded and multidimensional information of the urban canyon in NU helped to describe the dense morphology in Fully-developed space, and the RMSE further decreased by 0.36 °C (Fig. 13c). In Normal space, the improvements of UHI from 1U to NU was gradual and continuous, the RMSE declined 0.16 °C per simulation.

3.4.2. The comparison of the modeled UHI distribution in the four simulations

In the above analysis, we conducted a complete comparison of the UHI model performance with contrasting UCP configurations, based on 25 urban stations in the observation network. In this section, we will explore the distribution difference of UHI intensity for the whole urban area in the four simulations. To display the UHI intensity more clearly, this comparison was carried out for the hour with the maximum UHI effect (UHImax), which was also representative of the whole modeled period.

The selection approach of the typical hour is summarized in Fig. 14. First, according to the daily UHI summary from 25 urban stations, we
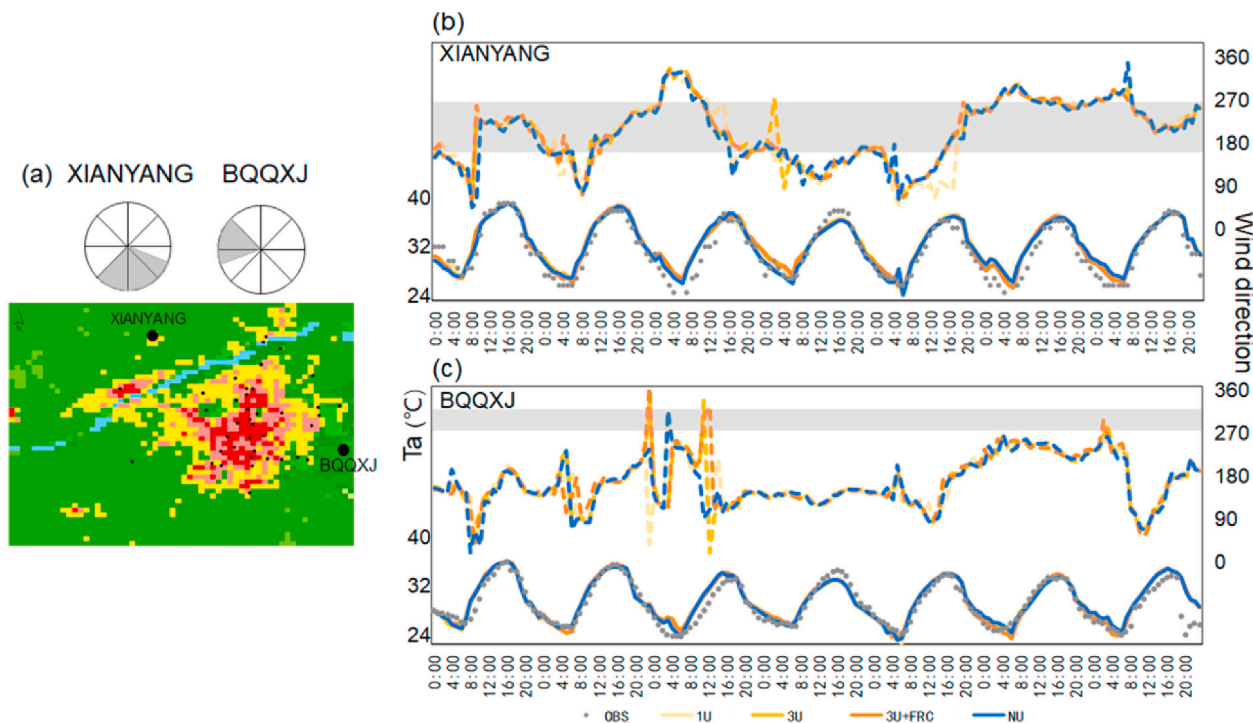

Fig. 12. The overview of qualified rural station selection: (a) The location of the XIANYANG and the BQQXJ station. When the rural station was downwind of the city, the wind direction is marked in grey. (b) and (c) are time series of hourly modeled wind direction and Ta in four simulations from July 19–25, 2018, for XIANYANG and BQQXJ respectively. The shaded areas infer the wind direction that transferred urban heat advection to the rural stations. See Fig. 5 for site locations.
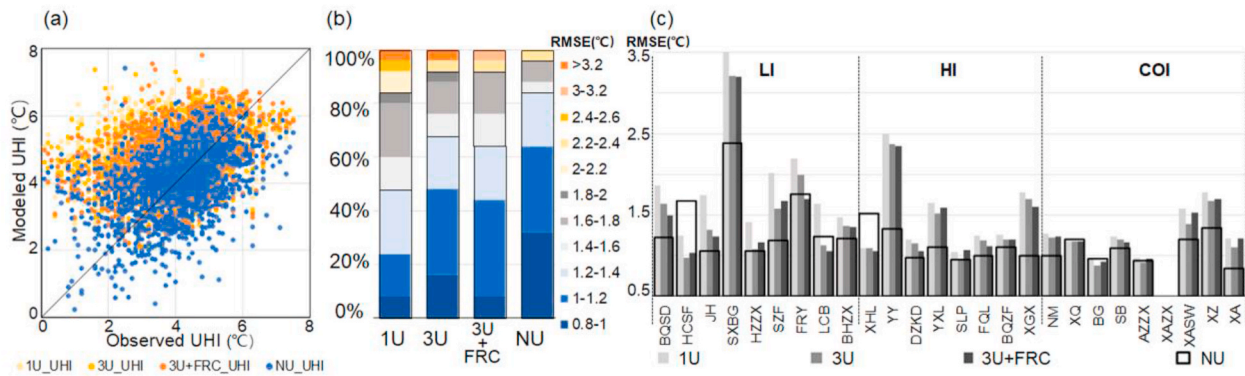
Fig. 13. The comparison of UHI modeled performance in four simulations: (a) the comparison of modeled UHI with observed UHI. (b) Cumulative relative frequency indicates the result of the hierarchical evaluation of all stations, according to their bias analysis. Stations with large errors (RMSE>2 °C) are yellow, stations with medium errors (1.4 °C < RMSE<2 °C) are grey, and stations with minor errors (RMSE<1.4 °C) are blue. (c) All 25 urban stations were divided into three urban classes, the results of four simulations at each station are represented by bars of different colors. See Fig. 5 for site locations. (For interpretation of the references to color in this figure legend, the reader is referred to the Web version of this article.)

obtained a reference array with the information of the maximum modeled UHI intensity in each station. Then we marked these UHImax intensities in red. The 24 h in all of the days spanning the simulation period were examined until we found the hour with the most red marks. In this case, the UHI intensity on 2018/7/21 at 2:00 LST was the most consistent with the reference array and could be identified as the typical hour.

The spatial distribution characteristics of modeled UHI were varied among the four simulations (Fig. 15). The modeled UHI was most prominent in 1U, most areas in the city experiencing a UHI of more than 4.5 °C. It is worth mentioning that the high-UHI area where the UHI exceeded 5 °C occupied about 30% of the city surface area in 1U, which was much larger than the actual situation in Xi'an. We could infer that the overestimation of UHI was caused by the uniform UCP configuration in 1U, and the use of the three land-use subdivisions in 3U and 3U + FRC partly modify it. In 3U, the range of high-UHI areas were limited to the downtown area and extended along a north-south axis across the city. The similar distribution of UHI appeared in 3U + FRC with weakening effects, and the UHI intensity of the suburban area located in the north-east declined by 2 °C (Fig. 15). However, the UHI effects were still overestimated, especially in the northern and western areas that mainly consisted of developing spaces or urban-rural transitional areas. These areas were sparsely built and highly covered with impervious material, which was mainly classified as LI and HI land-use according to the value of FRC_URB. Obviously, the urban canyons of these areas were much more open than recorded in the table, which led to substantial over-estimations of the UHI. Therefore, the gridded UCPs in NU played an

important role in the accurate modeling of UHI effects in these areas. In NU, the modeled UHI intensity became more reasonable and decreased by 0.5–2 °C in most areas. The high-UHI area shrank to the downtown area and the dense high-rise residential area in the south, which was more consistent with the actual situation in Xi'an (Fig. 15).

4. Discussion

In this study, gradual improvements were shown for the WRF/SLUCM model with contrasting UCP configurations. We found that the increased accuracy in UCPs brought about gradual and overall improvements of UHI and Ta, and had relatively slight effects for $\rho\nu$ and WP. These results were consistent with earlier studies dedicated to improving the modeled Ta performance in WRF/SLUCM using the subdivision of the urban land-use types [14–16] or 17 LCZ classes [24, 34], and by taking the value of the urban fraction in the mosaic approach [16,26] or gridded dataset [25]. Our results present a complete process of model performance comparison, in which the UCP configuration goes from a land-use table to a gridded dataset. Furthermore, the above comparisons are not limited to the widely concerned Ta but include other surface variables synchronously, which might provide references for studies on comprehensive indicators such as human thermal comfort.

Since we focused on the 2-m meteorological conditions, the evaluation of model performance only involved four surface climate variables. Some studies state that other indicators, such as wind profiles and the boundary layer height [17,22], are also sensitive to the accuracy of UCPs. Thus, the comparison of model performance from these
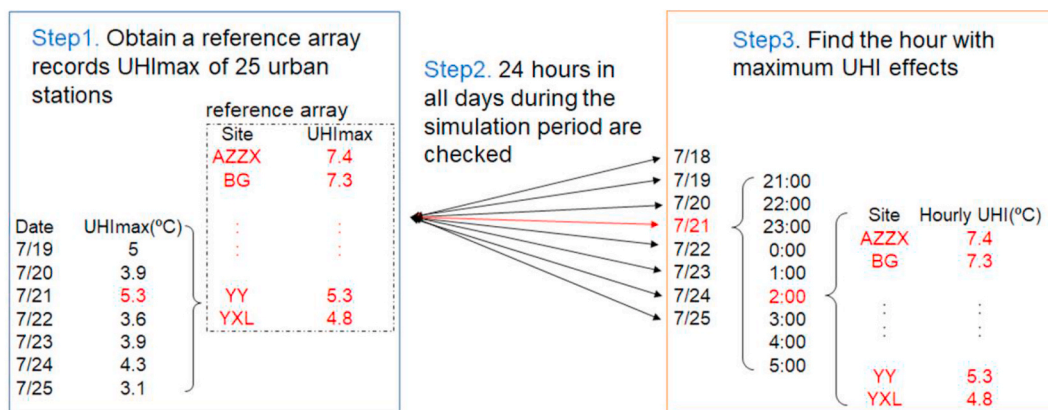

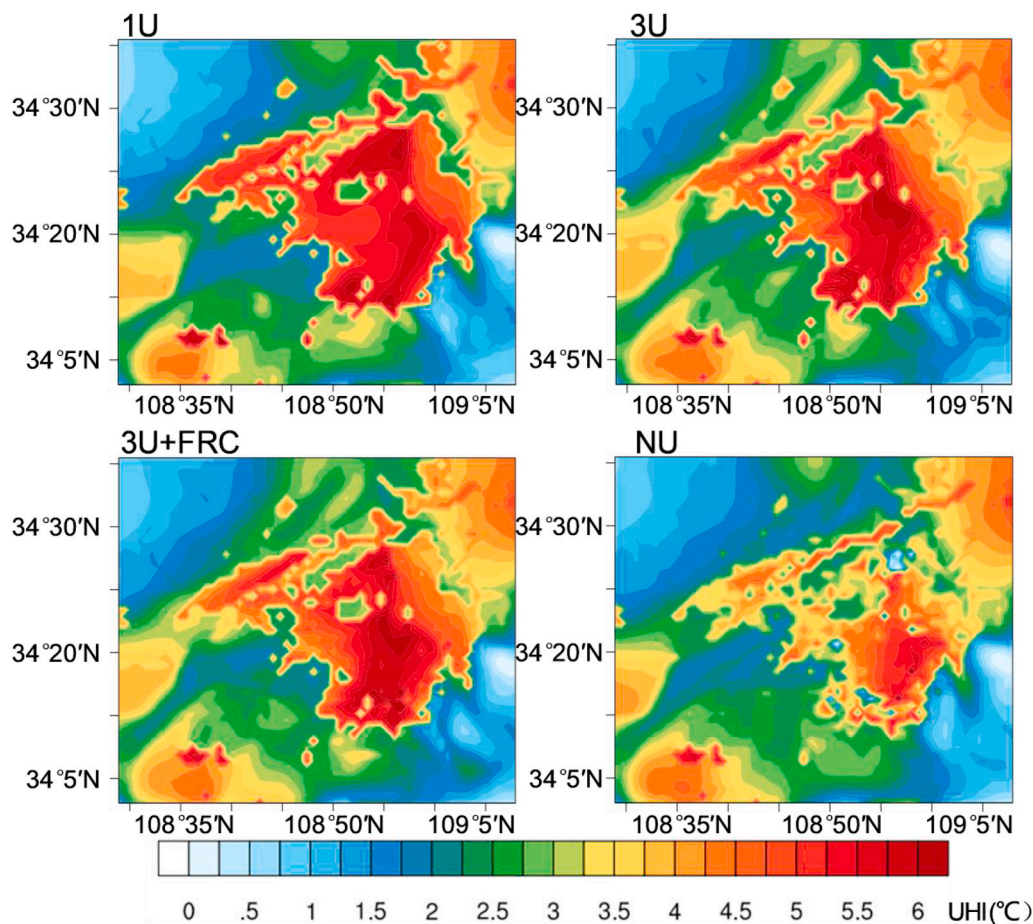**Fig. 14.** Overview of the selection of the representative hour for maximum UHI effect estimation.

Fig. 15. The modeled UHI distribution in four simulations, at LST 2018.7.21 2:00 a.m., which is the hour with maximum UHI effects.

perspectives deserves further study. This study only explores the model performance using the MRF scheme, which is widely used in the WRF/SLUCM model. Comparing improvements of fine-resolution UCPs in other boundary-layer schemes, such as the Shin-Hong 'scale-aware' scheme designed for sub-kilometer transition scales [35], would be an excellent follow-up to the current study.

Finally, it is noteworthy to mention that the improvements may vary within the study area and modeled seasons [26]. We would like to underline that this study only explored the model sensitivity for Xi'an, which is an inland city with a hot and dry summer. Thus, our results are more suitable for cities with a similar climate background. The conclusion may be different for coastal cities or cities with large-scale open water bodies where evaporation [25] and sea breeze [36] need to be considered. Moreover, Xi'an as a typical Chinese city has abundant and complex urban spaces, which is reflected in the observational stations used in this study (Table 3). This means that its urban morphology is hard to classify into a few categories, which leads to the obvious improvements in model performance with gridded UCPs. According to our results for Normal space, we could infer that the optimized effect may be weaker for a city with more uniform and homogeneous morphology. Therefore, other cities with different urban characteristics could infer the appropriate UCP configuration based on our results of station-by-station evaluations, which might provide a general reference.

5. Conclusion

In this study, we compared the performance of the WRF/SLUCM model in contrasting levels of UCP configurations and the results were evaluated using a high-density observational network of surface variables in Xi'an. We found that the temperature-related indicators such as

Ta and UHI were substantially sensitive to the UCP refinement. The improved effects of detailed UCP inputs were determined, which specifies the urban fraction and accurately reforms the urban canopy geometry in the model. A more realistic grid-scale turbulent energy portioning was calculated to reduce the warm bias in temperature, especially during the night. Overall, the improvements in surface wind and humidity were relatively limited.

In addition, the efficiencies of the improvements noted above were explored using station-to station bias analyses and we found variations in different urban spatial categories. Generally, the spaces with special morphology were more sensitive to the input accuracy of UCPs. For example, the areas highly covered by vegetation (Green space) and areas with open forms (Bare land Space) showed constant sensitivity to the increasing refinements of UCPs. The most significant improvement was seen using the input of gridded urban fraction, which accurately specified the surface evapotranspiration in these areas. The dense area (Fully-developed space) and areas with complex and mixture morphology (Mixed space) had better results using the gridded UCPs in the NUDAPT approach, which provided more detailed parameterizations of canyon geometry. The Normal space which was widely distributed in the urban area showed relatively small but continuous optimizations in UCP refinement.

Although limited spaces in the city exhibit special forms, it is important to note that these areas always presented differently in thermal environments and wind fields. The cooling effects seen in urban parks and elevated temperatures in dense areas may have a strong influence that spans kilometers over the surrounding areas. Therefore, the improvement in these spaces by applying high-resolution UCPs could also help accurately estimate the thermal distribution in the whole urban area.

Declaration of competing interest

The authors declare no competing financial interest.

Acknowledgements

Appendix A. Supplementary data

Supplementary data to this article can be found online at https://doi.org/10.1016/j.buildenv.2020.107109.

References

[1] I. Khaliq, C. Hof, R. Prinzinger, K. Böhning-Gaese, M. Pfenninger, Global variation in thermal tolerances and vulnerability of endotherms to climate change, Proc. Biol. Sci. 281 (1789) (2014) 20141097, https://doi.org/10.1098/rspb.2014.1097.

[2] T. Oke, The energetic basis of the urban heat island, Q. J. R. Meteorol. Soc. 108 (455) (1982) 1–24, https://doi.org/10.1002/qj.49710845502.

[3] T. Oke, Street design and urban canopy layer climate, Energy Build. 11 (1–3) (1988) 103–113, https://doi.org/10.1016/0378-7788(88)90026-6.

[4] P. Moonen, T. Defraeye, V. Dorer, B. Blocken, J. Carmeliet, Urban Physics: effect of the micro-climate on comfort, health and energy demand, Frontiers of Architectural Research 1 (3) (2012) 197–228, https://doi.org/10.1016/j.foar.2012.05.002.

[5] T. Kjellstrom, I. Holmer, B. Lemke, Workplace heat stress, health and productivity – an increasing challenge for low and middle-income countries during climate change, Glob. Health Action 2 (1) (2009) 2047, https://doi.org/10.3402/gha.v2i0.2047.

[6] G. Manoli, S. Fatichi, M. Schläpfer, K. Yu, T. Crowther, N. Meili, P. Burlando, G. Katul, E. Bou-Zeid, Magnitude of urban heat islands largely explained by climate and population, Nature 573 (7772) (2019) 55–60, https://doi.org/10.1038/s41586-019-1512-9.

[7] T.R. Oke, G. Mills, A. Christen, J.A. Voogt, Urban Climates, Cambridge University Press, Cambridge, 2017, https://doi.org/10.1017/9781139016476.

[8] P. Mirzaei, F. Haghighat, Approaches to study urban heat island – abilities and limitations, Build. Environ. 45 (10) (2010) 2192–2201, https://doi.org/10.1016/j.buildenv.2010.04.001.

[9] P. Mirzaei, Recent challenges in modeling of urban heat island, Sustainable Cities and Society 19 (2015) 200–206, https://doi.org/10.1016/j.scs.2015.04.001.

[10] F. Chen, H. Kusaka, R. Bornstein, J. Ching, C. Grimmond, S. Grossman-Clarke, T. Loridan, K. Manning, A. Martilli, S. Miao, D. Sailor, F. Salamanca, H. Taha, M. Tewari, X. Wang, A. Wyszogrodzki, C. Zhang, The integrated WRF/urban modelling system: development, evaluation, and applications to urban environmental problems, Int. J. Climatol. 31 (2) (2011) 273–288, https://doi.org/10.1002/joc.2158.

[11] J. Powers, Numerical prediction of an antarctic severe wind event with the weather research and forecasting (WRF) model, Mon. Weather Rev. 135 (9) (2007) 3134–3157, https://doi.org/10.1175/MWR3459.1.

[12] W.C. Skamarock, J.B. Klemp, J. Dudhia, D.O. Gill, D.M. Barker, W. Wang, J.G. Powers, A Description of the Advanced Research WRF Version 2(No. NCAR/TN-468+STR), University Corporation for Atmospheric Research, 2005, https://doi.org/10.5065/D6DZ069T.

[13] H. Kusaka, H. Kondo, Y. Kikegawa, F. Kimura, A simple single-layer urban canopy model for atmospheric models: comparison with multi-layer and slab models, Boundary-Layer Meteorol. 101 (3) (2001) 329–358, https://doi.org/10.1023/A:1019207923078.

[14] F. Chen, H. Kusaka, M. Tewari, J.-W. Bao, H. Hirakuchi, Utilizing the Coupled WRF/LSM/Urban Modeling System with Detailed Urban Classification to Simulate the Urban Heat Island Phenomena over the Greater Houston Area, Paper 9.11, American Meteorological Society Fifth Symposium on the Urban Environment, Vancouver, British Columbia, 2004, 23-27 August 2004.

[15] H. Li, Y. Zhou, X. Wang, X. Zhou, H. Zhang, S. Sodoudi, Quantifying urban heat island intensity and its physical mechanism using WRF/UCM 650, Science of The Total Environment, 2019, pp. 3110–3119, https://doi.org/10.1016/j.scitotenv.2018.10.025.

[16] A. Sharma, H. Fernando, A. Hamlet, J. Hellmann, M. Barlage, F. Chen, Urban meteorological modeling using WRF: a sensitivity study, Int. J. Climatol. 37 (4) (2016) 1885–1900, https://doi.org/10.1002/joc.4819.

[17] S. Lee, S. Kim, W. Angevine, L. Bianco, S. McKeen, C. Senff, M. Trainer, S. Tucker, R. Zamora, Evaluation of urban surface parameterizations in the WRF model using measurements during the Texas Air Quality Study 2006 field campaign, Atmos. Chem. Phys. 11 (5) (2011) 2127–2143, https://doi.org/10.5194/acp-11-2127-2011.

[18] J. Mao, J. Yang, A. Afshari, L. Norford, Global sensitivity analysis of an urban microclimate system under uncertainty: design and case study, Build. Environ. 124 (2017) 153–170, https://doi.org/10.1016/j.buildenv.2017.08.011.

[19] A. Salvati, M. Palme, G. Chiesa, M. Kolokotroni, Built form, urban climate and building energy modelling: case-studies in Rome and Antofagasta, Journal of Building Performance Simulation 13 (2) (2020) 209–225, https://doi.org/10.1080/19401493.2019.1707876.

[20] A. Adelia, C. Yuan, L. Liu, R. Shan, Effects of urban morphology on anthropogenic heat dispersion in tropical high-density residential areas, Energy Build. 186 (2019) 368–383, https://doi.org/10.1016/j.enbuild.2019.01.026.

[21] T. Glotfelty, M. Tewari, K. Sampson, M. Duda, F. Chen, J. Ching, NUDAPT 44 Documentation, 2013.

[22] F. Salamanca, A. Martilli, M. Tewari, F. Chen, A study of the urban boundary layer using different urban parameterizations and high-resolution urban canopy parameters with WRF, Journal of Applied Meteorology and Climatology 50 (5) (2011) 1107–1128, https://doi.org/10.1175/2010JAMC2538.1.

[23] E. Gutiérrez, J. González, A. Martilli, R. Bornstein, M. Arend, Simulations of a heat-wave event in New York city using a multilayer urban parameterization, Journal of Applied Meteorology and Climatology 54 (2) (2015) 283–301, https://doi.org/10.1175/JAMC-D-14-0028.1.

[24] O. Brousse, A. Martilli, M. Foley, G. Mills, B. Bechtel, WUDAPT, an efficient land use producing data tool for mesoscale models? Integration of urban LCZ in WRF over Madrid, Urban Climate 17 (2016) 116–134, https://doi.org/10.1016/j.uclim.2016.04.001.

[25] A. Monaghan, L. Hu, N. Brunsell, M. Barlage, O. Wilhelmi, Evaluating the impact of urban morphology configurations on the accuracy of urban canopy model temperature simulations with MODIS, J. Geophys. Res.: Atmosphere 119 (11) (2014) 6376–6392, https://doi.org/10.1002/2013JD021227.

[26] B. Jänicke, F. Meier, D. Fenner, U. Fehrenbach, A. Holtmann, D. Scherer, Urban-rural differences in near-surface air temperature as resolved by the Central Europe Refined analysis (CER): sensitivity to planetary boundary layer schemes and urban canopy models, Int. J. Climatol. 37 (4) (2016) 2063–2079, https://doi.org/10.1002/joc.4835.

[27] X. Zhang, G. Steeneveld, D. Zhou, C. Duan, A. Holtslag, A diagnostic equation for the maximum urban heat island effect of a typical Chinese city: a case study for Xi'an, Build. Environ. 158 (2019) 39–50, https://doi.org/10.1016/j.buildenv.2019.05.004.

[28] Xi'an Statistics Bureau, Xi'an Statistical Yearbook 2017, Xi'an Press, 2017.

[29] M. Gao, H. Shen, X. Han, H. Li, L. Zhang, Multiple timescale analysis of the urban heat island effect based on the Community Land Model: a case study of the city of Xi'an, China, Environ. Monit. Assess. 190 (1) (2017), https://doi.org/10.1007/s10661-017-6320-9.

[30] L. Yu, J. Wang, P. Gong, Improving 30 m global land-cover map FROM-GLC with time series MODIS and auxiliary data sets: a segmentation-based approach, Int. J. Rem. Sens. 34 (16) (2013) 5851–5867, https://doi.org/10.1080/01431161.2013.798055.

[31] J.P. Wang, et al., Sensitivity analysis of urbanization and anthropogenic heat impacts on meteorological factors in Xi'an[J], Drought weather 33 (3) (2015) 434–443.

[32] R. Macdonald, Modelling the mean velocity profile in the urban canopy layer, Boundary-Layer Meteorol. 97 (1) (2000) 25–45, https://doi.org/10.1023/A:1002785830512.

[33] hui Zhang, gang Wang, jia-ji Pan, Analysis of observational data difference between DZZ4 and ZQZ-CII automatic meteorological stations 10, Xiandai Nongye Keji, 2015, pp. 231–233.

[34] K. Hammerberg, O. Brousse, A. Martilli, A. Mahdavi, Implications of employing detailed urban canopy parameters for mesoscale climate modelling: a comparison between WUDAPT and GIS databases over Vienna, Austria, Int. J. Climatol. 38 (2018) e1241–e1257, https://doi.org/10.1002/joc.5447.

[35] H. Shin, S. Hong, Representation of the subgrid-scale turbulent transport in convective boundary layers at gray-zone resolutions, Mon. Weather Rev. 143 (1) (2015) 250–271, https://doi.org/10.1175/MWR-D-14-00116.1.

[36] X. Li, T. Koh, D. Entekhabi, M. Roth, J. Panda, L. Norford, A multi-resolution ensemble study of a tropical urban environment and its interactions with the background regional atmosphere, J. Geophys. Res.: Atmosphere 118 (17) (2013) 9804–9818, https://doi.org/10.1002/jgrd.50795.